Salomäki, J., Hinkkanen, M., and Luomi, J. (2006). Sensorless control of induction motor drives equipped with inverter output filter. IEEE Transactions on Industrial Electronics, 53 (4), pp. 1188-1197.

Sensorless Control of Induction Motor Drives Equipped With Inverter Output Filter

Janne Salomäki, *Student Member, IEEE*, Marko Hinkkanen, *Member, IEEE*, and Jorma Luomi, *Member, IEEE*

***Abstract*—This paper deals with the speed sensorless vector control of an induction motor in a special case where the output voltage of the pulsewidth-modulated inverter is filtered by an inductance–capacitance (LC) filter. The system states are estimated by means of an adaptive full-order observer, and no additional voltage, current, or speed measurements are needed. The rotor speed adaptation is based on the estimation error of the inverter output current. Quasi-steady-state and linearization analyses are used to design an observer that enables a wide operation region, including very low and very high speeds. A torque-maximizing control method is applied in the field-weakening region. Simulation and experimental results show that the performance is comparable to that of a drive without the LC filter.**

***Index Terms*—Adaptive full-order observer, induction motor (IM) drives, inverter output filter, speed sensorless, vector control.**

I. Introduction

THE OUTPUT voltage of a pulsewidth-modulated (PWM) inverter consists of sharp-edged voltage pulses, which cause unwanted effects in the motor drive. Sudden alterations of the voltage produce high voltage stresses in motor insulations and may cause bearing currents [1], [2]. Harmonics at the switching frequency and its multiples give rise to additional losses and acoustic noise. These phenomena can be reduced by adding an inductance–capacitance (LC) filter to the output of the PWM inverter. When the filter is connected between the inverter and the motor, the motor control becomes more difficult. The stator current differs from the measured inverter output current, and problems may also be encountered because of the filter resonance. Therefore, the dynamics of the filter should be taken into account when implementing a vector control method.

Only few publications deal with the vector control of ac motors fed through an LC filter. These control methods are usually based on extra current or voltage measurements, and a speed sensor is used [3]–[5]. For practical reasons, however, no extra hardware should be added to the frequency converter, and the drive should preferably work without a speed sensor. A full-order observer was recently presented for induction motor (IM) drives with an LC filter [6], which allows the estimation of the motor current and voltage without additional current or voltage measurements. The control of the system is based on cascaded control loops.

Manuscript received March 18, 2005; revised January 15, 2006. Abstract published on the Internet May 18, 2006. This work was supported in part by ABB Oy and in part by the Walter Ahlström Foundation.

The authors are with the Power Electronics Laboratory, Helsinki University of Technology, FI-02015 TKK, Espoo, Finland (e-mail: janne.salomaki@tkk.fi).

Digital Object Identifier 10.1109/TIE.2006.878314

In this paper, a speed sensorless method is proposed for the vector control of IM drives with an LC filter. The full-order observer [6] is augmented with a speed adaptation mechanism, resulting in a drive where only the inverter output current and the dc-link voltage are measured [7]. The observer is analyzed using current loci in quasi-steady state and a linearized model. Emphasis is put on the operation in a wide speed range. The low-speed operation is stabilized by means of a modified speed-adaptation law in the regenerating mode, and the high-speed operation is made possible by means of a speed-dependent observer gain. Furthermore, a torque-maximizing field-weakening method is applied, ensuring good performance even at the highest speeds.

II. System Model and Control

Fig. 1(a) shows the variable-speed drive system. Space-vector notation is used for three-phase quantities. The inverter output voltage $\underline{u}_A$ is filtered by an LC filter, and the IM is fed by the filtered voltage $\underline{u}_s$. The inverter output current $\underline{i}_A$ and the dc-link voltage u_{dc} are the only measured quantities, whereas the stator voltage $\underline{u}_s$, the stator current $\underline{i}_s$, and the electrical angular speed ω_m of the rotor are estimated by an observer. The topology of the three-phase LC filter is shown in Fig. 1(b), where L_f is the inductance and R_{Lf} is the series resistance of the inductor, and C_f is the capacitance of the filter.

A. System Model

In a reference frame rotating at an angular frequency ω_k, the state-space representation of the system, which consists of the IM and the LC filter, can be written as

$$\frac{d\underline{\boldsymbol{x}}}{dt} = \underline{\mathbf{A}}\,\underline{\boldsymbol{x}} + \mathbf{B}\underline{u}_A \tag{1}$$

$$\underline{i}_A = \mathbf{C}\underline{\boldsymbol{x}} \tag{2}$$

where $\underline{\boldsymbol{x}} = [\underline{i}_A \;\; \underline{u}_s \;\; \underline{i}_s \;\; \underline{\psi}_R]^T$ is the state vector. The matrix transpose is denoted by the superscript T, and the rotor flux linkage is represented by $\underline{\psi}_R$. The system matrices in (1) and (2) are

$$\underline{\mathbf{A}} = \begin{bmatrix} -\frac{R_{Lf}}{L_f} & -\frac{1}{L_f} & 0 & 0 \\ \frac{1}{C_f} & 0 & -\frac{1}{C_f} & 0 \\ 0 & \frac{1}{L'_s} & -\frac{1}{\tau'_\sigma} & \frac{1}{L'_s}\left(\frac{1}{\tau_r} - j\omega_m\right) \\ 0 & 0 & R_R & -\frac{1}{\tau_r} + j\omega_m \end{bmatrix} - j\omega_k\mathbf{I} \tag{3}$$

$$\mathbf{B} = \begin{bmatrix} \frac{1}{L_f} & 0 & 0 & 0 \end{bmatrix}^T \tag{4}$$

$$\mathbf{C} = \begin{bmatrix} 1 & 0 & 0 & 0 \end{bmatrix} \tag{5}$$

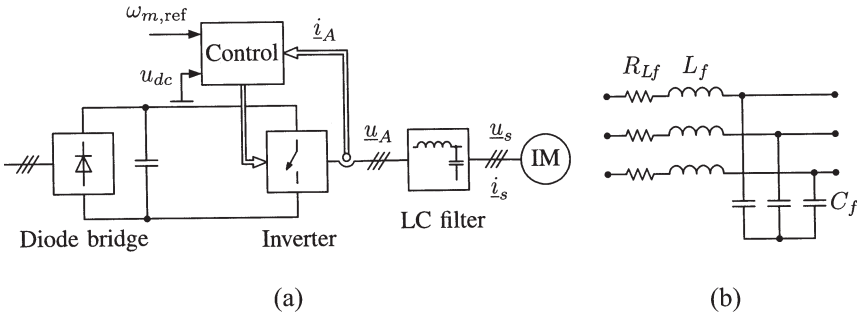

Fig. 1. (a) Variable-speed drive system. (b) Three-phase LC filter.

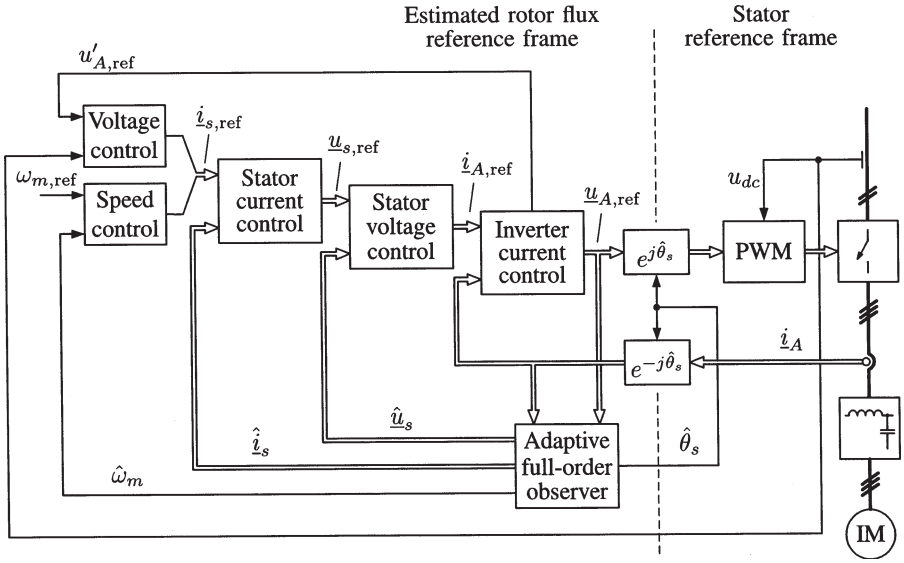

Fig. 2. Simplified block diagram of rotor-flux-oriented control system. Space vectors on the left-hand side of coordinate transformations are in the estimated rotor flux reference frame and on the right-hand side in the stator reference frame. Double lines indicate complex quantities (space vectors), whereas single lines indicate real quantities (scalars).

where $\mathbf{I}$ is a 4×4 identity matrix. Corresponding to the inverse-Γ model of the IM [8], R_s and R_R are the stator and rotor resistances, respectively, L'_s is the stator transient inductance, and L_M the magnetizing inductance. The two time constants are defined as $\tau'_\sigma = L'_s/(R_s + R_R)$ and $\tau_r = L_M/R_R$.

The electromagnetic torque is

$$T_e = \frac{3}{2} p \,\mathrm{Im}\left\{\underline{i}_s \underline{\psi}^*_R\right\} \tag{6}$$

where p is the number of pole pairs, and the symbol * denotes the complex conjugate. The equation of motion is

$$\frac{d\omega_m}{dt} = \frac{p}{J}(T_e - T_L) - \frac{b}{J}\omega_m \tag{7}$$

where J is the total moment of inertia, T_L is the load torque, and b is the viscous friction coefficient.

B. Control System

Fig. 2 shows a simplified block diagram of the control system (the estimated quantities being marked by the $\hat{}$). The cascade control and the speed-adaptive full-order observer are implemented in the estimated rotor flux reference frame, i.e., in a reference frame where $\underline{\hat{\psi}}_R = \hat{\psi}_R + j0$ and ω_k equals the angular frequency $\hat{\omega}_s$ of the estimated rotor flux. The angle of the estimated rotor flux, which is denoted by $\hat{\theta}_s$, is obtained by integrating $\hat{\omega}_s$.

The innermost control loop in the cascade control governs the inverter current $\underline{i}_A$ by means of a proportional–integral (PI) controller. The stator voltage $\underline{u}_s$ is governed by a PI controller in the next control loop. In both control loops, cross couplings caused by the rotating reference frame are compensated. Fig. 3 shows a signal flow diagram of the inverter current and stator voltage controllers.

The motor control forms the outermost control loops in Fig. 2. The stator current $\underline{i}_s$ and the rotor speed ω_m are controlled by PI controllers. The stator current control also includes a compensation of the cross-coupling and the back electromotive force (EMF). A voltage controller is used for adjusting the rotor flux so that the voltage required by the inverter current controller matches the voltage capability of the inverter. The voltage control algorithm is described in Section V.

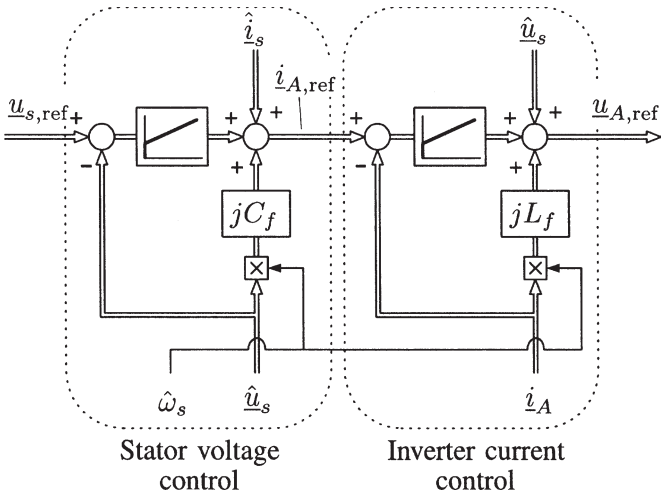

Fig. 3. Signal flow diagram of stator voltage and inverter current controllers.

III. Speed-Adaptive Full-Order Observer

A. Observer Structure

Speed-adaptive full-order observers are viable estimation methods for speed sensorless IM drives [9], [10]. For a drive with an LC filter, the number of observer states has to be increased, and the inverter current is the measured state instead of the stator current. The electrical angular speed of the rotor, which is included in the state-space representation (1), is estimated using an adaptation mechanism. The observer, which is implemented in the estimated rotor flux reference frame, is defined by

$$\frac{d\hat{\underline{\boldsymbol{x}}}}{dt} = \hat{\underline{\mathbf{A}}}\,\hat{\underline{\boldsymbol{x}}} + \mathbf{B}\underline{u}_A + \underline{\mathbf{K}}(\underline{i}_A - \hat{\underline{i}}_A) \tag{8}$$

where the system matrix and the observer gain vector are

$$\hat{\underline{\mathbf{A}}} = \begin{bmatrix} -\frac{R_{Lf}}{L_f} & -\frac{1}{L_f} & 0 & 0 \\ \frac{1}{C_f} & 0 & -\frac{1}{C_f} & 0 \\ 0 & \frac{1}{L'_s} & -\frac{1}{\tau'_\sigma} & \frac{1}{L'_s}\left(\frac{1}{\tau_r} - j\hat{\omega}_m\right) \\ 0 & 0 & R_R & -\frac{1}{\tau_r} + j\hat{\omega}_m \end{bmatrix} - j\hat{\omega}_s\mathbf{I} \tag{9}$$

$$\underline{\mathbf{K}} = [\,\underline{k}_1 \quad \underline{k}_2 \quad \underline{k}_3 \quad \underline{k}_4\,]^T. \tag{10}$$

The conventional speed-adaptation law [9] is modified for the case where an LC filter is used. The estimation error of the inverter current is used for the speed adaptation (instead of the estimation error of the stator current). To stabilize the regenerating-mode operation at low speeds, the idea of a rotated current estimation error is adopted [11]. The speed-adaptation law in the estimated rotor flux reference frame is

$$\hat{\omega}_m = -K_p\,\mathrm{Im}\left\{(\underline{i}_A - \hat{\underline{i}}_A)e^{-j\phi}\right\} - K_i\int \mathrm{Im}\left\{(\underline{i}_A - \hat{\underline{i}}_A)e^{-j\phi}\right\}dt \tag{11}$$

where K_p and K_i are nonnegative adaptation gains, and the angle ϕ changes the direction of the error projection. The digital implementation of the adaptive full-order observer is based on a simple symmetric Euler method [12].

TABLE I
Parameters of the Motor and the LC Filter

Motor Parameters	
Stator resistance R_s	3.67 Ω
Rotor resistance R_R	1.65 Ω
Stator transient inductance L'_s	0.0209 H
Magnetizing inductance L_M	0.264 H
Total moment of inertia J	0.0155 kgm^2
Rated speed	1430 r/min
Rated current (rms)	5.0 A
Rated torque	14.6 Nm
LC Filter Parameters	
Inductance L_f	8.0 mH
Capacitance C_f	9.9 μF
Series resistance R_{Lf}	0.1 Ω

B. Quasi-Steady-State Analysis

The dynamics of the estimation error $\underline{\boldsymbol{e}} = \underline{\boldsymbol{x}} - \hat{\underline{\boldsymbol{x}}}$ are obtained from (1) and (8) as follows:

$$\frac{d\underline{\boldsymbol{e}}}{dt} = (\underline{\mathbf{A}} - \underline{\mathbf{K}}\mathbf{C})\underline{\boldsymbol{e}} + (\underline{\mathbf{A}} - \hat{\underline{\mathbf{A}}})\hat{\underline{\boldsymbol{x}}} \tag{12}$$

$$\underline{i}_A - \hat{\underline{i}}_A = \mathbf{C}\underline{\boldsymbol{e}} \tag{13}$$

where the difference between system matrices is

$$\underline{\mathbf{A}} - \hat{\underline{\mathbf{A}}} = \underbrace{\begin{bmatrix} 0 & 0 & 0 & 0 \\ 0 & 0 & 0 & 0 \\ 0 & 0 & 0 & -j\frac{1}{L'_s} \\ 0 & 0 & 0 & j \end{bmatrix}}_{\underline{\mathbf{M}}}(\omega_m - \hat{\omega}_m) \tag{14}$$

when accurate parameter estimates are assumed. For the quasi-steady-state analysis, the derivative of estimation error (12) is set to zero. This assumption is reasonable if the speed estimation error $e_\omega = \omega_m - \hat{\omega}_m$ is changing much slower than the estimation error $\underline{\boldsymbol{e}}$.

The operating point is determined by the synchronous angular frequency ω_s, the slip angular frequency $\omega_r = \omega_s - \omega_m$, and the estimated rotor flux $\hat{\psi}_R$. The parameters of a 2.2-kW four-pole IM (400 V, 50 Hz) and an LC filter, which are used for the following analysis, are given in Table I. The base values of the angular frequency, current, and voltage are $2\pi \cdot 50$ rad/s, $\sqrt{2} \cdot 5.0$ A, and $\sqrt{2/3} \cdot 400$ V, respectively.

Fig. 4 illustrates the current estimation error as the slip angular frequency is varied from the negative rated slip to the positive rated slip for various values of the rotor speed estimation error e_ω. The rated slip angular frequency is $\omega_{rN} = 0.05$ per unit (p.u.), the synchronous angular frequency is $\omega_s = 0.1$ p.u., and the estimated rotor flux is constant. The observer gain is $\underline{\mathbf{K}} = [3000\ \mathrm{s}^{-1}\ 0\ 0\ 0]^T$.

Fig. 4(a) illustrates the case where $\phi = 0$ in the adaptation law (11). The rotor speed estimate is calculated using only the imaginary part (q component) of the current estimation

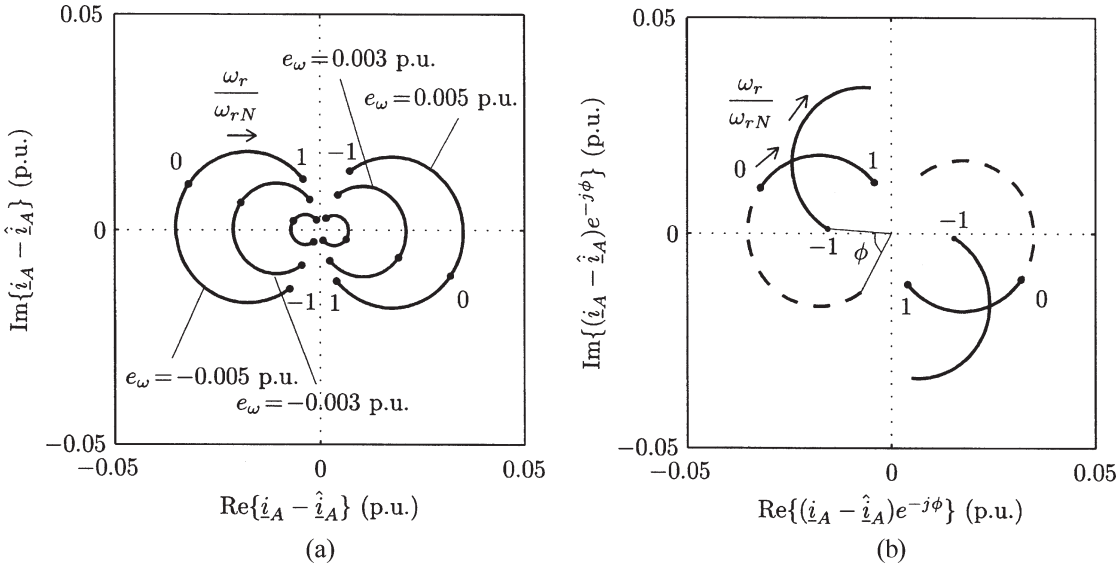

Fig. 4. Loci of current estimation error as slip angular frequency varies from $-\omega_{rN}$ to ω_{rN}. (a) Original error for various rotor speed estimation error values between -0.005 and 0.005 p.u. (b) Error rotated by $\phi = 0.367\pi$ at negative slip angular frequencies (only for rotor speed estimation error values of -0.005 and 0.005 p.u.). The synchronous angular frequency is $\omega_s = 0.1$ p.u., and the reference frame is fixed to the estimated rotor flux.

error. This kind of adaptation law works well in the motoring mode (where $\omega_s\omega_r > 0$), but at low synchronous speeds in the regenerating mode ($\omega_s\omega_r < 0$), the imaginary part of the current estimation error changes its sign at a certain slip angular frequency as can be seen in Fig. 4(a). Beyond this point, the estimated rotor speed is corrected to the wrong direction, leading to unstable operation. This problem is encountered only at low synchronous speeds.

The unstable operation can be avoided if the real part of the current estimation error is also taken into account in the speed adaptation. Correspondingly, the current estimation error is rotated by a factor $e^{-j\phi}$. The angle is selected as [11]

$$\phi = \begin{cases} \phi_{\max}\mathrm{sign}(\hat{\omega}_s)\left(1 - \frac{|\hat{\omega}_s|}{\omega_\phi}\right), & \text{if } |\hat{\omega}_s| < \omega_\phi \text{ and } \hat{\omega}_s\hat{\omega}_r < 0 \\ 0, & \text{otherwise} \end{cases} \tag{15}$$

where $\phi_{\max}$ is the maximum correction angle, and ω_ϕ is the limit for the synchronous angular frequency after which the correction is not used. The influence of the angle correction is illustrated in Fig. 4(b) for the values $\phi_{\max} = 0.414\pi$ and $\omega_\phi = 0.85$ p.u. The estimated rotor speed is now properly corrected in the regenerating mode. The quasi-steady-state analysis does not guarantee the stability of the speed-adaptive observer, but it can be used for selecting the parameters $\phi_{\max}$ and ω_ϕ.

C. Linearization Analysis

The dynamic behavior of the speed-adaptive observer near an equilibrium can be studied via small-signal linearization. Linearizing the estimation error dynamics (12) leads to

$$\frac{d\tilde{\underline{e}}}{dt} = (\underline{\mathbf{A}}_0 - \underline{\mathbf{K}}_0\mathbf{C})\tilde{\underline{e}} + \underline{\mathbf{M}}\,\underline{\boldsymbol{x}}_0(\tilde{\underline{\omega}} - \tilde{\hat{\underline{\omega}}}) \tag{16}$$

where the subscript 0 denotes operating-point quantities, and tilde marks deviations about the operating point, e.g., the deviation in the rotor speed is $\tilde{\omega}_m = \omega_m - \omega_{m0}$.

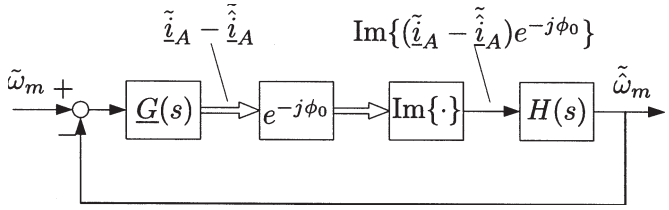

Fig. 5. Signal flow diagram of linearized model.

It is worth noticing that $\hat{\omega}_{m0} = \omega_{m0}$ and $\underline{\boldsymbol{e}}_0 = 0$ in the steady-state operating point when accurate parameter estimates are assumed. Hence, the linearized dynamics (12) of the estimation error are independent of the deviations in the synchronous angular frequency $\tilde{\omega}_s$. The linearization in (16) holds even if the observer gain $\underline{\mathbf{K}}$ is a function of $\hat{\omega}_s$ or $\hat{\omega}_m$.

The transfer function from the speed estimation error to the inverter current estimation error obtained from (16) is

$$\begin{aligned} \underline{G}(s) &= \frac{\tilde{\underline{i}}_A(s) - \tilde{\hat{\underline{i}}}_A(s)}{\tilde{\omega}_m(s) - \tilde{\hat{\omega}}_m(s)} \\ &= \mathbf{C}(s\mathbf{I} - \underline{\mathbf{A}}_0 + \underline{\mathbf{K}}_0\mathbf{C})^{-1}\underline{\mathbf{M}}\,\underline{\boldsymbol{x}}_0. \end{aligned} \tag{17}$$

Based on (11), the transfer function from the imaginary part of the rotated current estimation error to the speed estimate is $H(s) = -K_p - K_i/s$. The resulting linearized model is shown in Fig. 5. This model is used for investigating the pole locations of the linearized system at different operating points. The motor and filter parameters given in Table I are used for the following analysis. The speed adaptation gains were selected based on the linearization analysis and simulations: $K_p = 10\ (\mathrm{A}\cdot\mathrm{s})^{-1}$ and $K_i = 20\,000\ (\mathrm{A}\cdot\mathrm{s}^2)^{-1}$.

The observer gain $\underline{\mathbf{K}}$ affects the stability of the system. In an IM drive without an LC filter, an adaptive observer can be stable in the motoring mode even with zero gain. However, zero gain cannot be used when an LC filter is present. Fig. 6(a) shows the poles of the linearized model as the synchronous

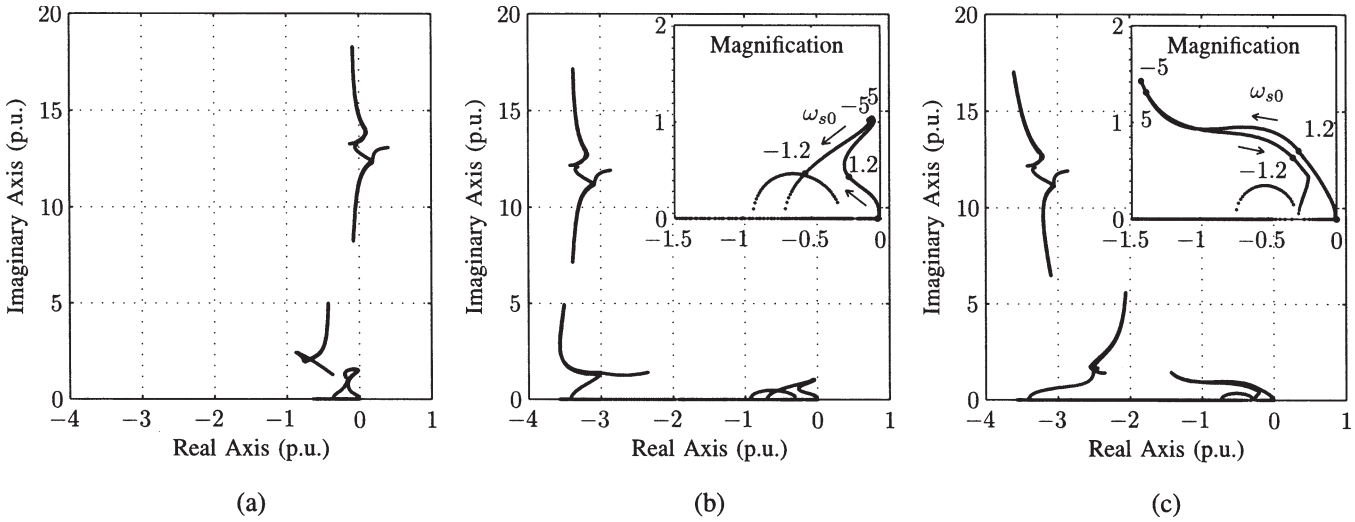

Fig. 6. Poles of linearized model as synchronous angular frequency ω_{s0} is varied from -5 to 5 p.u., and slip angular frequency is 0.05 p.u. Observer gain is (a) $\underline{\mathbf{K}} = [0\ 0\ 0\ 0]^T$. (b) $\underline{\mathbf{K}} = [3000\ \mathrm{s}^{-1}\ 0\ 0\ 0]^T$. (c) Proposed gain.

angular frequency ω_{s0} varies from -5 to 5 p.u., and the slip angular frequency equals its rated value. The adaptive observer with zero gain becomes unstable both in the motoring and generating modes, which corresponds to the poles in the right half-plane.

A simple observer gain, which is proposed in [7], is given by

$$\underline{\mathbf{K}} = [k_1 \quad 0 \quad 0 \quad 0]^T. \tag{18}$$

Fig. 6(b) shows the poles obtained using (18) with $k_1 = 3000\ \mathrm{s}^{-1}$. All poles stay in the left half-plane; but at higher frequencies, the damping of the dominant poles is poor.

The observer performance can be enhanced at high frequencies by adding a speed-dependent complex-valued gain component $\underline{k}_4$ in a fashion similar to a speed-adaptive flux observer in an IM drive without the LC filter [13]. The proposed observer gain is

$$\underline{\mathbf{K}} = [k_1 \quad 0 \quad 0 \quad \lambda\{-1 + j\,\mathrm{sign}(\hat{\omega}_m)\}]^T \tag{19}$$

where

$$\lambda = \begin{cases} \lambda' \frac{|\hat{\omega}_m|}{\omega_\lambda}, & \text{if } |\hat{\omega}_m| < \omega_\lambda \\ \lambda', & \text{if } |\hat{\omega}_m| \geq \omega_\lambda \end{cases}. \tag{20}$$

The positive constants λ' and ω_λ can be selected based on the linearization analysis. The observer gain component $\underline{k}_4$ also has an effect on the results of the quasi-steady-state analysis, but the parameters $\phi_{\max}$ and ω_ϕ chosen for the gain (18) can be directly used for the proposed gain. Fig. 6(c) shows the poles obtained using (19) with $k_1 = 3000\ \mathrm{s}^{-1}$, $\lambda' = 10\ \mathrm{V \cdot A}^{-1}$, and $\omega_\lambda = 1$ p.u. All poles stay in the left half-plane, and the damping of the dominant poles is adequate in the whole inspected operation region.

IV. Inverter Limitations

The maximum torque developed by the motor depends on the inverter and motor current limits, as well as on the maximum voltage of the inverter. In steady state, the torque (6) of the IM can be expressed as

$$T_e = \frac{3}{2} p L_M i_{sd} i_{sq} \tag{21}$$

where i_{sd} is the d (flux producing) component of the stator current in the rotor flux reference frame, and i_{sq} is the q (torque producing) component.

In this section, the effects of the inverter limitations on the stator current components are analyzed when an LC filter is present. It is assumed that the inverter current is limited according to $|\underline{i}_A| \leq i_{A,\max}$, and the motor current limit is omitted for simplicity. In addition, the filter and stator resistances are ignored since their effects are small at higher speeds.

A. Current Limit

The inverter current components i_{Ad} and i_{Aq} are limited by the maximum current $i_{A,\max}$ according to

$$i_{Ad}^2 + i_{Aq}^2 \leq i_{A,\max}^2. \tag{22}$$

The steady-state solution of (1) yields the stator current as a function of the inverter current

$$i_{sd} = \frac{i_{Ad}}{1 - \omega_s^2 C_f (L_s' + L_M)} \tag{23}$$

$$i_{sq} = \frac{i_{Aq}}{1 - \omega_s^2 C_f L_s'}. \tag{24}$$

According to (22)–(24), the feasible stator current has an elliptical boundary as shown in Fig. 7(a). At low speeds, this ellipse approaches a circle, and the inverter and stator currents are approximately equal in steady state. If the LC filter is not used, the current limit boundary is a circle.

B. Voltage Limit

The dc-link voltage determines the maximum voltage that the inverter can supply. Omitting the possible overmodulation, the

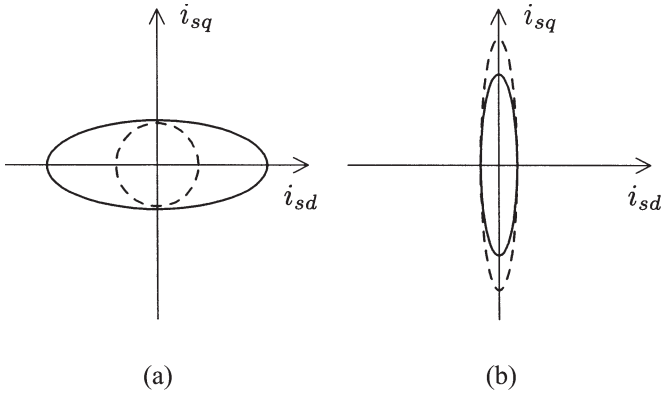

Fig. 7. Feasible stator current as (a) inverter current is limited and (b) inverter voltage is limited. Solid lines are for a drive with an LC filter and dashed lines for a drive without a filter.

maximum inverter output voltage $u_{A,\max}$ is $u_{dc}/\sqrt{3}$, and the inverter voltage components u_{Ad} and u_{Aq} are limited by

$$u_{Ad}^2 + u_{Aq}^2 \leq u_{A,\max}^2. \tag{25}$$

The steady-state solution of (1) gives for the stator current components

$$i_{sd} = \frac{u_{Aq}}{\omega_s \left(L_f + L'_s + L_M\right) - \omega_s^3 C_f L_f \left(L'_s + L_M\right)} \tag{26}$$

$$i_{sq} = \frac{u_{Ad}}{-\omega_s \left(L_f + L'_s\right) + \omega_s^3 C_f L_f L'_s}. \tag{27}$$

The voltage limit affects the stator current according to (25)–(27). A drive with an LC filter has a smaller voltage limit ellipse than a drive without a filter as shown in Fig. 7(b).

V. Torque-Maximizing Field-Weakening Control

The steady-state torque of an IM drive with an LC filter is governed by (21) with the constraints (22)–(27). Field weakening is necessary at high speeds due to the voltage limitation. A conventional field-weakening method reduces the rotor flux reference proportional to $1/\omega_m$, as the angular speed of the rotor exceeds a speed limit for the field-weakening control. More advanced methods are based on a voltage control and enable maximum torque operation [14]–[16]. In the following, the method presented in [16] is applied to a drive equipped with an LC filter.

A. Control Algorithm

The field weakening is included in the voltage controller shown in Fig. 2. The control algorithm is

$$\frac{di_{sd,\mathrm{ref}}}{dt} = \gamma_f \left[u_{A,\max}^2 - \left(u'_{A,\mathrm{ref}}\right)^2\right], \quad i_{sd,\mathrm{ref}} \leq i_{sd,N} \tag{28}$$

where $i_{sd,\mathrm{ref}}$ is the d component of the stator current reference, γ_f is the controller gain, $u'_{A,\mathrm{ref}}$ is the magnitude of the unlimited inverter voltage reference, and $i_{sd,N}$ is the nominal d component of the stator current.

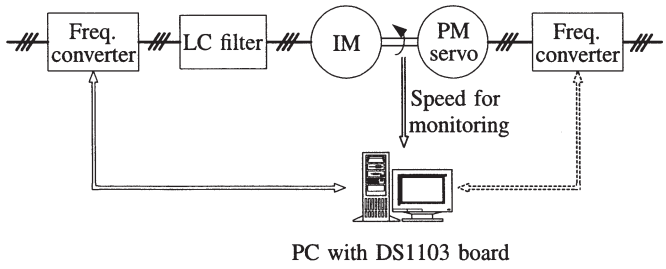

Fig. 8. Experimental setup. Speed sensorless control of the IM is investigated, and the permanent magnet (PM) servo motor is used as the loading machine.

The speed controller output, i.e., the q component of the stator current reference, is limited according to

$$i_{sq,\mathrm{ref}} = \min\left\{\left|i'_{sq,\mathrm{ref}}\right|, \sqrt{\frac{i_{A,\max}^2 - \left[1-\hat{\omega}_s^2 C_f \left(L'_s + L_M\right)\right]^2 i_{sd,\mathrm{ref}}^2}{1-\hat{\omega}_s^2 C_f L'_s}}, \frac{\hat{\psi}_R}{L_f + L'_s} + i_{sd,\mathrm{ref}}\right\} \mathrm{sign}\left(i'_{sq,\mathrm{ref}}\right). \tag{29}$$

The minimum of the three values is chosen, i.e., 1) the absolute value of the unlimited reference $i'_{sq,\mathrm{ref}}$; 2) the value defined by the inverter current limit according to (22)–(24); or 3) the value maximizing the torque (21) constrained by the inverter voltage limit according to (25)–(27) with the approximations $L_f + L'_s + L_M \gg \omega_s^2 C_f L_f (L'_s + L_M)$ and $L_f + L'_s \gg \omega_s^2 C_f L_f L'_s$.

B. Gain Selection

Desired closed-loop dynamics are obtained for the rotor flux by selecting the gain γ_f. It is assumed that the dynamics of the rotor flux are slow compared with the dynamics of the inverter current, stator voltage, and stator current. In the rotor flux reference frame, the steady-state solution of the fast dynamics—the first three equations in (1)—is approximately

$$u_{Ad} \approx (R_s + R_R) i_{sd} - \left(L_f + L'_s\right) \omega_s i_{sq} - \frac{1}{\tau_r}\psi_R \tag{30}$$

$$u_{Aq} \approx \left(L_f + L'_s\right) \omega_s i_{sd} + (R_s + R_R) i_{sq} + \omega_m \psi_R. \tag{31}$$

When these approximations are used, the linearization of (28) results in

$$\frac{d\tilde{i}_{sd}}{dt} = -2\gamma_{f0} u_{A,\max} \left(L_f + L'_s\right) \omega_{s0} \tilde{i}_{sd} - 2\gamma_{f0} u_{A,\max} \omega_{s0} \tilde{\psi}_R \tag{32}$$

where the following approximations have been made: $i_{sd,\mathrm{ref}} = i_{sd}$, $R_s = 0$, $u_{Ad0} = 0$, and $u_{Aq0} = u_{A,\max}$. The open-loop rotor flux dynamics are

$$\frac{d\tilde{\psi}_R}{dt} = R_R \tilde{i}_{sd} - \frac{1}{\tau_r}\tilde{\psi}_R. \tag{33}$$

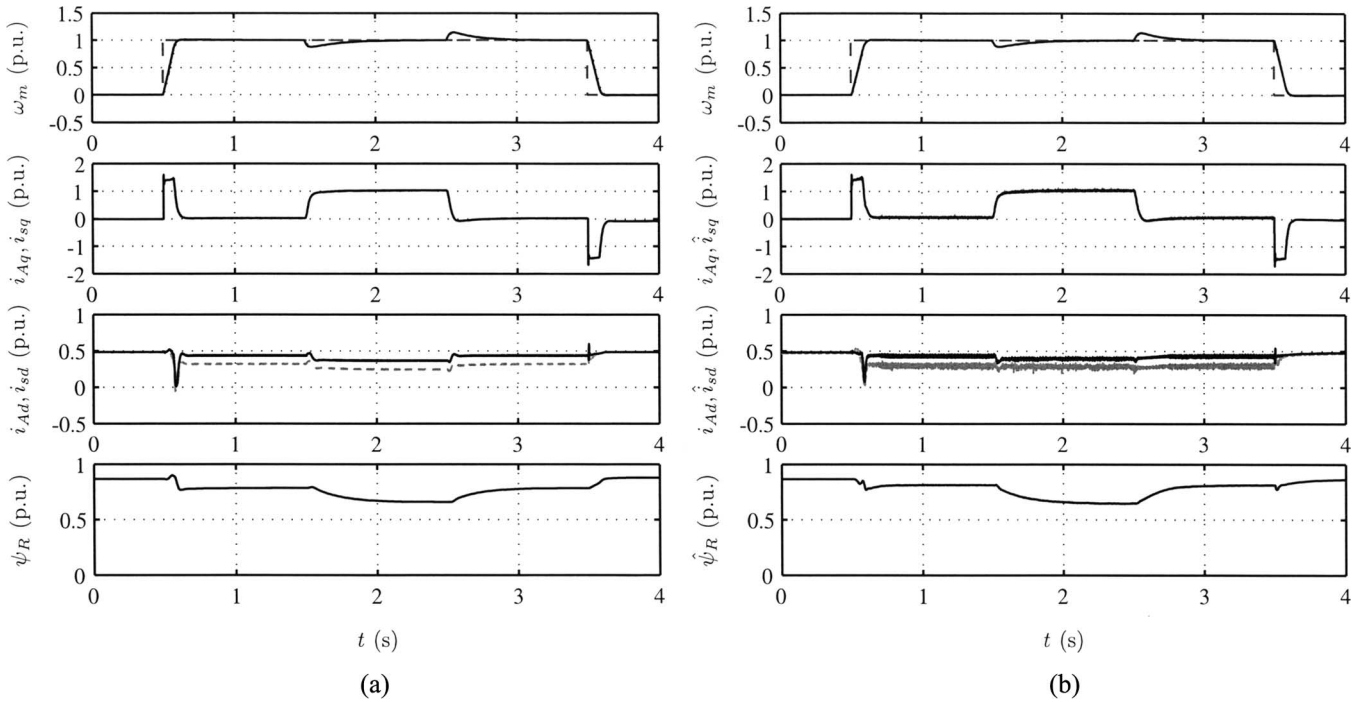

Fig. 9. (a) Simulation and (b) experimental results showing a sequence with speed and load changes. The first subplot shows the speed reference (dashed) and the actual rotor speed (solid) and its estimate (dotted). The second subplot shows the q components of the stator (solid) and inverter (dashed) currents. The third subplot shows the d components of the stator (solid) and inverter (dashed) currents. The fourth subplot shows the rotor flux magnitude.

The gain γ_f can be selected by placing the poles of the system (32) and (33) approximately to $(-1 \pm \mathrm{j})R_R/(L_f + L'_s)$. The result is

$$\gamma_f = \frac{R_R}{u_{A,\max}\left(L_f + L'_s\right)^2 \omega'_s} \tag{34}$$

where the flux reduction in the field-weakening region is taken into account by

$$\omega'_s = \begin{cases} \omega_\gamma, & \text{if } |\hat{\omega}_s| \le \omega_\gamma \\ |\hat{\omega}_s|, & \text{otherwise} \end{cases}. \tag{35}$$

An approximate angular speed limit for the field weakening is denoted by ω_γ.

VI. Simulation and Experimental Results

The control method was investigated by means of computer simulations and experiments. The MATLAB/Simulink software was used for the simulations. The experimental setup is illustrated in Fig. 8. The 2.2-kW four-pole IM was fed by a frequency converter controlled by a dSPACE DS1103 PPC/DSP board. The parameters of the experimental setup correspond to those given in Table I. The dc-link voltage was measured, and the reference voltage $\underline{u}_{A,\mathrm{ref}}$ was used in the observer as shown in Fig. 2. The rotor speed was measured only for monitoring purposes. Simple current feedforward compensation for dead times and power device voltage drops was applied [17]. A PM servo motor was used as the loading machine.

The sampling frequency was equal to the switching frequency of 5 kHz. The bandwidths of the controllers were $2\pi \cdot 500$ rad/s for the inverter current, $2\pi \cdot 250$ rad/s for the stator voltage, $2\pi \cdot 150$ rad/s for the stator current, and $2\pi \cdot 7.5$ rad/s for the rotor speed. The speed estimate was filtered using a low-pass filter having the bandwidth of $2\pi \cdot 40$ rad/s. The integrator windup of the PI controllers was prevented by applying a back-calculation method similar to [7]. The parameters of the observer gain (19) were $k_1 = 3000\ \mathrm{s}^{-1}$, $\lambda' = 10\ \mathrm{V \cdot A}^{-1}$, and $\omega_\lambda = 1$ p.u. The parameters used in the speed adaptation were $K_p = 10\ (\mathrm{A \cdot s})^{-1}$, $K_i = 20\,000\ (\mathrm{A \cdot s}^2)^{-1}$, $\phi_{\max} = 0.414\pi$, and $\omega_\phi = 0.85$ p.u. The parameter used in (35) was $\omega_\gamma = 0.85$ p.u. The inverter current limit was $i_{A,\max} = 1.5$ p.u.

Fig. 9(a) shows simulation results obtained for a sequence consisting of a speed reference step from zero to 1 p.u. at $t = 0.5$ s, a rated load torque step at $t = 1.5$ s, a load torque removal at $t = 2.5$ s, and a deceleration to standstill at $t = 3.5$ s. The corresponding experimental results are shown in Fig. 9(b). The q components of the inverter and stator currents are nearly equal. As expected, the d component of the inverter current is lower than that of the stator current especially at high speeds. The measured performance corresponds well to the simulation results.

Fig. 10 shows a magnification of the speed reference step in Fig. 9. The transient response behaves well: The rotor accelerates rapidly, and the speed estimate is close to the actual speed. The inverter and stator voltage and current waveforms are shown in detail in Fig. 11. The stator voltage and current are nearly sinusoidal.

Fig. 12 shows experimental results obtained for zero-speed reference when rated load torque is applied at $t = 2$ s, reversed at $t = 6$ s, and removed at $t = 10$ s. This kind of a sequence is challenging for speed sensorless drives even without the LC filter.

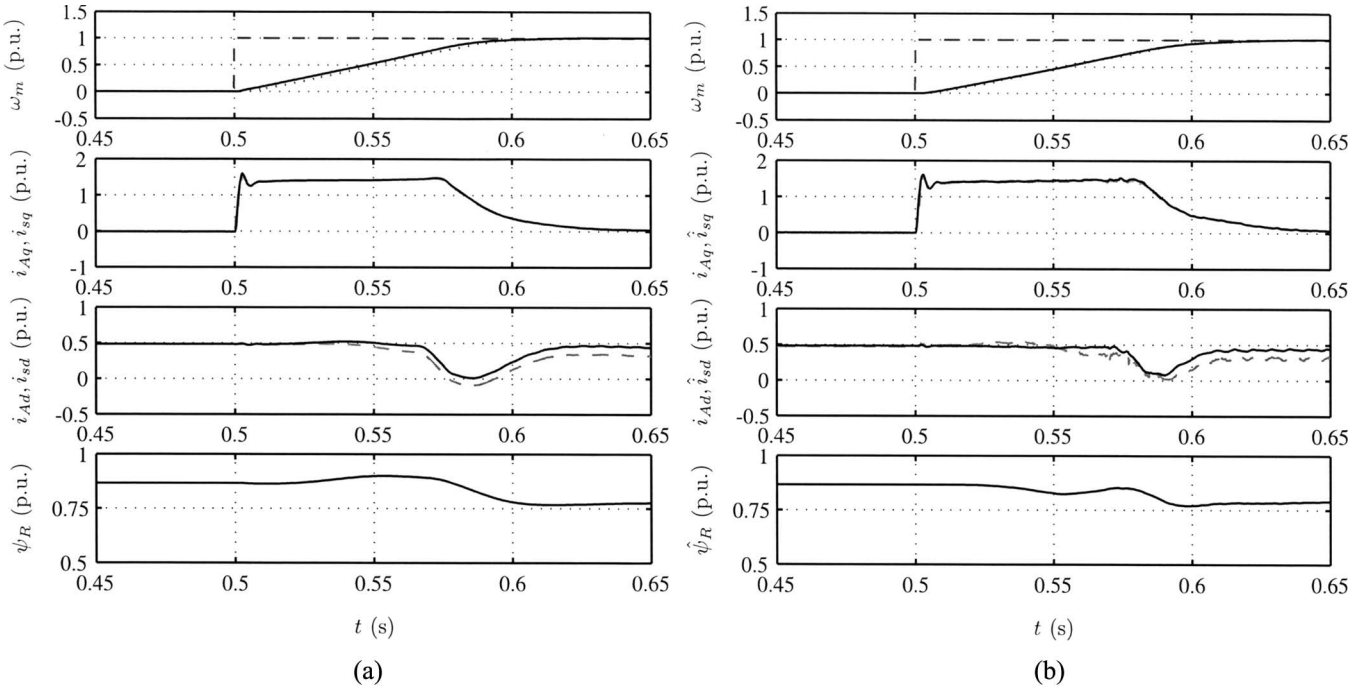

Fig. 10. Magnification of simulation and experimental results shown in Fig. 9. (a) Simulation. (b) Experiment.

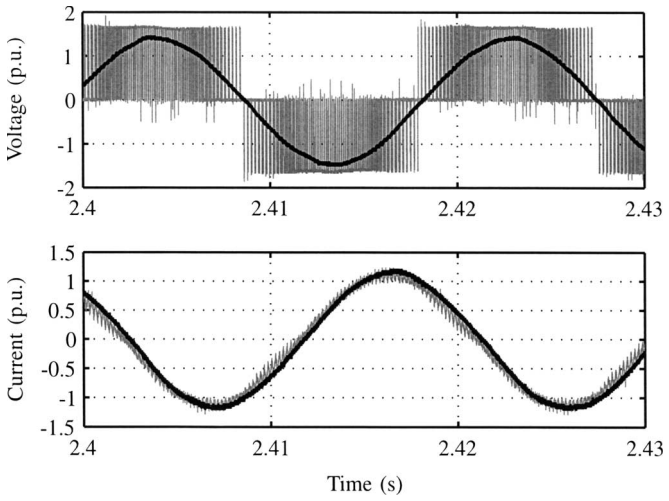

Fig. 11. Voltage and current waveforms from experiment in Fig. 9(b). The first subplot shows the inverter output voltage (phase to phase) and the stator voltage (phase to phase). The second subplot shows the inverter current and the stator current.

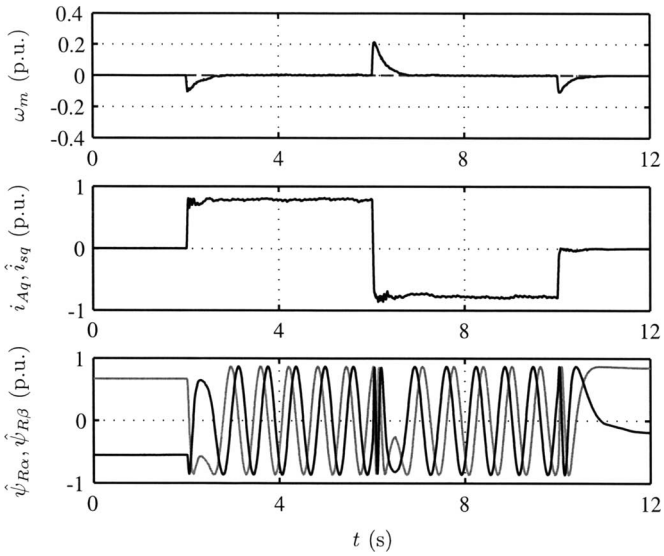

Fig. 12. Experimental results showing zero-speed operation under load. The first subplot shows the speed reference (dashed) and the actual rotor speed (solid) and its estimate (dotted). The second subplot shows the q components of the stator (solid) and inverter (dashed) currents. The third subplot shows the real and imaginary components of the rotor flux in the stator reference frame.

Fig. 13 shows experimental results obtained for a slow torque reversal as the speed reference is kept constant at 0.1 p.u. The drive operates first in the motoring mode until $t = 7.5$ s and the rest of the sequence in the regenerating mode. Without the angle correction in the speed-adaptation law (11), the drive became unstable soon after the transition to the regenerating mode. The frequency of the oscillations in Fig. 13 is the six-fold synchronous frequency. These oscillations originate from inverter nonlinearities and are emphasized in the regenerating mode as the voltage is very low.

Fig. 14 shows experimental results obtained for a slow speed reversal under rated load torque. The drive operates first in the motoring mode until $t = 7.5$ s, then a short period in the plugging mode, and finally from about $t = 7.9$ s in the regenerating mode. The system remains stable, although some oscillations appear in the regenerating-mode operation at low speeds. Slower speed reversals at rated load resulted in larger oscillations or unstable operation, but extremely slow reversals were successful at no load.

Fig. 15 shows experimental results obtained for an acceleration from zero speed to 3 p.u. at no load. The voltage controller decreases the d component of the stator current reference, resulting in a fast reduction in the rotor flux. The d component

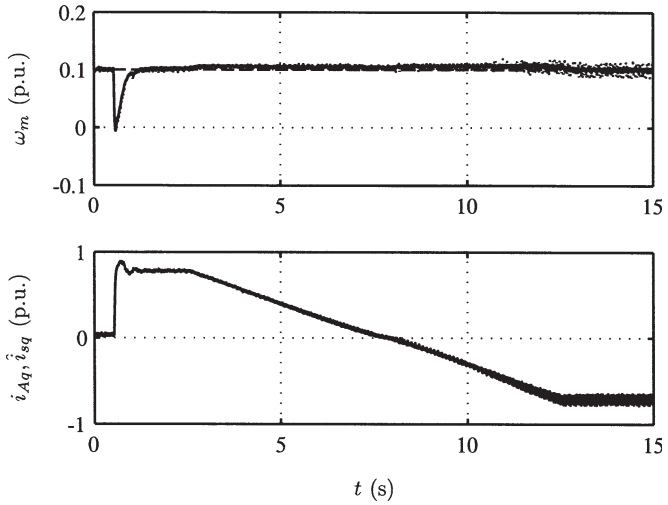

Fig. 13. Experimental results showing a slow load torque reversal. The first subplot shows the speed reference (dashed) and the actual rotor speed (solid) and its estimate (dotted). The second subplot shows the q components of the stator (solid) and inverter (dashed) currents.

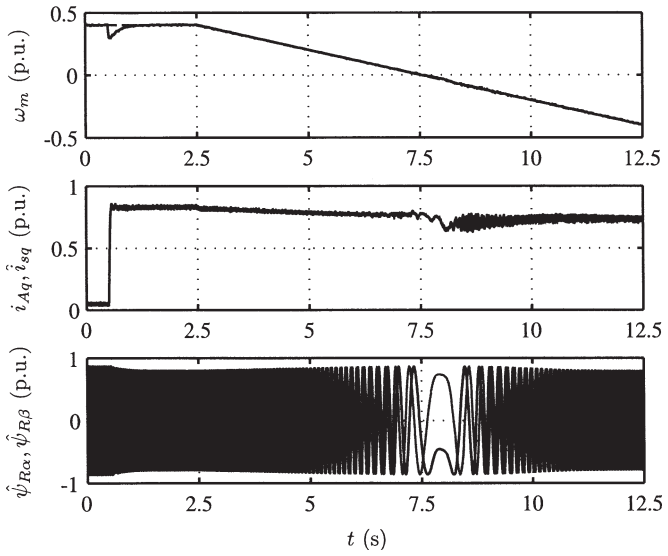

Fig. 14. Experimental results showing a slow speed reversal. The explanations of the curves are as in Fig. 12.

of the inverter current is negative at high speeds as the filter capacitor supplies more magnetizing current than required by the motor.

VII. Conclusion

When the inverter output voltage is filtered by an LC filter, the speed sensorless vector control of an IM can be based on cascaded control loops and an adaptive full-order observer. Only the inverter output current and the dc-link voltage are measured. Hence, the control method makes it possible to add a filter to an existing drive, and no hardware modifications are needed in the frequency converter. The quasi-steady-state and linearization analyses are useful for designing an adaptive observer that operates in wide speed and load ranges, including zero speed under load. Even though the effects of the inverter limitations on the stator current differ from those

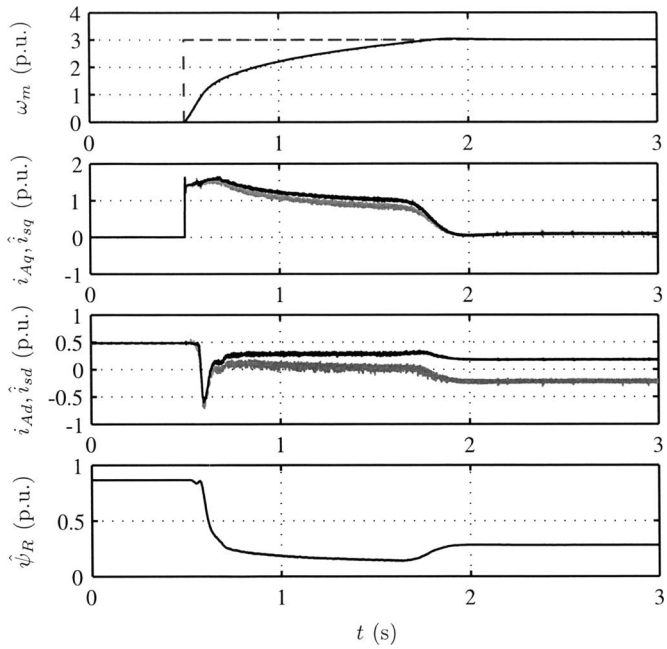

Fig. 15. Experimental results showing an acceleration from zero speed to 3 p.u. The explanations of the curves are as in Fig. 9.

of a drive without the LC filter, a similar torque-maximizing field-weakening control method can be used. Simulation and experimental results show that the proposed speed sensorless vector control method works properly and the performance is comparable to that of a drive without the LC filter.

Acknowledgment

The authors would like to thank the reviewers for their insightful comments and helpful suggestions.

References

[1] A. von Jouanne, P. Enjeti, and W. Gray, "The effect of long motor leads on PWM inverter fed AC motor drive systems," in *Proc. IEEE APEC*, Dallas, TX, Mar. 1995, vol. 2, pp. 592–597.

[2] D. F. Busse, J. M. Erdman, R. J. Kerkman, D. W. Schlegel, and G. L. Skibinski, "The effects of PWM voltage source inverters on the mechanical performance of rolling bearings," *IEEE Trans. Ind. Appl.*, vol. 33, no. 2, pp. 567–576, Mar./Apr. 1997.

[3] M. Kojima, K. Hirabayashi, Y. Kawabata, E. C. Ejiogu, and T. Kawabata, "Novel vector control system using deadbeat-controlled PWM inverter with output LC filter," *IEEE Trans. Ind. Appl.*, vol. 40, no. 1, pp. 162–169, Jan./Feb. 2004.

[4] A. Nabae, H. Nakano, and Y. Okamura, "A novel control strategy of the inverter with sinusoidal voltage and current outputs," in *Proc. IEEE PESC*, Taipei, Taiwan, R.O.C., Jun. 1994, vol. 1, pp. 154–159.

[5] R. Seliga and W. Koczara, "Multiloop feedback control strategy in sine-wave voltage inverter for an adjustable speed cage induction motor drive system," in *Proc. EPE*, Graz, Austria, Aug. 2001, CD-ROM.

[6] J. Salomäki and J. Luomi, "Vector control of an induction motor fed by a PWM inverter with output LC filter," in *Proc. NORPIE*, Trondheim, Norway, Jun. 2004, CD-ROM.

[7] J. Salomäki, M. Hinkkanen, and J. Luomi, "Sensorless vector control of an induction motor fed by a PWM inverter through an output LC filter," in *Proc. IPEC*, Niigata, Japan, Apr. 2005, CD-ROM, pp. 404–411.

[8] G. R. Slemon, "Modelling of induction machines for electric drives," *IEEE Trans. Ind. Appl.*, vol. 25, no. 6, pp. 1126–1131, Nov./Dec. 1989.

[9] H. Kubota, K. Matsuse, and T. Nakano, "DSP-based speed adaptive flux observer of induction motor," *IEEE Trans. Ind. Appl.*, vol. 29, no. 2, pp. 344–348, Mar./Apr. 1993.

[10] G. Yang and T.-H. Chin, "Adaptive-speed identification scheme for a vector-controlled speed sensorless inverter-induction motor drive," *IEEE Trans. Ind. Appl.*, vol. 29, no. 4, pp. 820–825, Jul./Aug. 1993.
[11] M. Hinkkanen and J. Luomi, "Stabilization of regenerating-mode operation in sensorless induction motor drives by full-order flux observer design," *IEEE Trans. Ind. Electron.*, vol. 51, no. 6, pp. 1318–1328, Dec. 2004.
[12] J. Niiranen, "Fast and accurate symmetric Euler algorithm for electromechanical simulations," in *Proc. Elecrimacs*, Lisbon, Portugal, Sep. 1999, vol. 1, pp. 71–78.
[13] M. Hinkkanen, "Analysis and design of full-order flux observers for sensorless induction motors," *IEEE Trans. Ind. Electron.*, vol. 51, no. 5, pp. 1033–1040, Oct. 2004.
[14] S.-H. Kim and S.-K. Sul, "Voltage control strategy for maximum torque operation of an induction machine in the field-weakening region," *IEEE Trans. Ind. Electron.*, vol. 44, no. 4, pp. 512–518, Aug. 1997.
[15] H. Grotstollen and J. Wiesing, "Torque capability and control of a saturated induction motor over a wide range of flux weakening," *IEEE Trans. Ind. Electron.*, vol. 42, no. 4, pp. 374–381, Aug. 1995.
[16] L. Harnefors, K. Pietiläinen, and L. Gertmar, "Torque-maximizing field-weakening control: Design, analysis, and parameter selection," *IEEE Trans. Ind. Electron.*, vol. 48, no. 1, pp. 161–168, Feb. 2001.
[17] J. K. Pedersen, F. Blaabjerg, J. W. Jensen, and P. Thøgersen, "An ideal PWM-VSI inverter with feedforward and feedback compensation," in *Proc. EPE*, Brighton, U.K., Sep. 1993, vol. 4, pp. 312–318.

Janne Salomäki (S'06) was born in Hyvinkää, Finland, in 1978. He received the M.Sc. (Eng.) degree from Helsinki University of Technology, Espoo, Finland, in 2003.

Since 2003, he has been with the Power Electronics Laboratory, Helsinki University of Technology, as a Research Scientist. His main research interest is the control of electrical drives.

Marko Hinkkanen (M'06) was born in Rautjärvi, Finland, in 1975. He received the M.Sc. (Eng.) and D.Sc. (Tech.) degrees from Helsinki University of Technology, Espoo, Finland, in 2000 and 2004, respectively.

Since 2000, he has been with the Power Electronics Laboratory, Helsinki University of Technology, as a Research Scientist. His main research interest is the control of electrical drives.

Jorma Luomi (M'92) was born in Helsinki, Finland, in 1954. He received the M.Sc. (Eng.) and D.Sc. (Tech.) degrees from Helsinki University of Technology, Espoo, Finland, in 1977 and 1984, respectively.

In 1980, he joined Helsinki University of Technology, and from 1991 to 1998, he was a Professor at Chalmers University of Technology. Since 1998, he has been a Professor in the Department of Electrical and Communications Engineering, Helsinki University of Technology. His research interests are in the areas of electric drives, electric machines, and numerical analysis of electromagnetic fields.